

Tilt Corrections for Normal Mode Observations on Ocean Bottom Seismic Data, an example from the PI-LAB experiment

Nicholas Harmon (1) *1,2, Gabi Laske (1)3, Wayne Crawford (1)4, Catherine A. Rychert (1)1,2

¹Ocean and Earth Science, University of Southampton, Southampton, UK, ²Geology and Geophysics, Woods Hole Oceanographic Institution, Woods Hole, MA, USA, ³Institute of Geophysics and Planetary Physics, Scripps Institution of Oceanography, La Jolla, CA, USA, ⁴Institut de Physique Du Globe De Paris, Centre National de la Recherche Scientifique, Paris, France

Author contributions: Conceptualization: N. Harmon, G. Laske, W. Crawford, C. A. Rychert. Funding Acquisition: N. Harmon, C. A. Rychert. Formal Analysis: N. Harmon, G. Laske, W. Crawford, C. A. Rychert. Writing – original draft: N. Harmon, G. Laske, W. Crawford, C. A. Rychert. Writing – review & editing: N. Harmon, G. Laske, W. Crawford, C. A. Rychert.

Abstract Earth's normal modes are fundamental observations used in global seismic tomography to understand Earth structure. Land seismic station coverage is sufficient to constrain the broadest scale Earth structures. However, 70% of Earth's surface is covered by the oceans, hampering our ability to observe variations in local mode frequencies that contribute to imaging small-scale structures. Broadband ocean bottom seismometers can record spheroidal modes to fill in gaps in global data coverage. Ocean bottom recordings are contaminated by signals from complex interactions between ocean and solid Earth dynamics at normal mode frequencies. We present a method for correcting tilt on broadband ocean bottom seismometers by rotation. The correction improves the ability of some instruments to observe spheroidal modes down to $_0$ S₄. We demonstrate this method using 15 broadband ocean bottom seismometers from the PI-LAB array. We measure normal mode peak frequency shifts and compare with 1-D reference mode frequencies and predictions from 3-D global models. Our measurements agree with the 3-D models for modes between $_0$ S₁₄ - $_0$ S₃₇ with small but significant differences. These differences likely reflect real Earth structure. This suggests incorporating ocean bottom normal mode measurements into global inversions will improve models of global seismic velocity structure.

Production Editor:
Gareth Funning
Handling Editor:
Danielle Sumy
Copy & Layout Editor:
Hannah F. Mark

Received: July 1 2022 Accepted: September 16 2022 Published: November 2 2022

1 Introduction

Earth's free oscillations or normal modes provide important seismic observational constraints on the Earth's elastic and anelastic structure from the core to the upper mantle (Masters and Widmer, 1995). These oscillations group into radial, spheroidal, and toroidal modes. Spherically averaged measurements of the frequency and width (or amplitude and phase) of mode spectral peaks observed after large earthquakes can be inverted to investigate the 1-D structure of the Earth (e.g., Gilbert and Dziewonski, 1975; Dziewonski and Anderson, 1981), while details of mode splitting reveal long-wavelength three-dimensional variations (Masters et al., 1982; Smith and Masters, 1989; Woodhouse and Dziewonski, 1984). Normal mode data can also be combined with other complementary seismic phases and waveforms to invert for higher resolution 3-D Earth models (e.g., Dziewonski and Anderson, 1981; Moulik and Ekström, 2014; Ritsema et al., 2011). At the lowest frequencies (f < 1 mHz) measurements of relatively few earthquakes on relatively few but nevertheless globally well-distributed very-broadband seismic stations suffice to sample the three-dimensional structure of the Earth reasonably well. However, observations of

land stations have been installed on many ocean islands, the ambient-noise conditions are sometimes less than ideal. In addition, ocean island coverage is sparse. The U.S.-operated global seismograph network (GSN) reached its design goal with maximum global coverage in 2004 with plans to expand GSN to more seafloor locations (Kohler et al., 2020), but many regions remain under-sampled (Butler et al., 2004). 70% of the Earth's surface is covered by oceans. Therefore, further progress in station coverage requires the deployment of ocean bottom seismometers (OBS). High-end very-broadband OBSs have been deployed in seafloor boreholes (Stephen et al., 2003) or buried cabled arrays (Duennebier et al., 2002) using ROVs. Alternatively, free-fall OBSs can be deployed on the seafloor from ships. In this case the instruments fall through the water and then record autonomously for about 1 year before returning to the surface for recovery. Typically, OBSs are deployed for targeted regional studies, using instrumentation that is often not sensitive to seismic signals at frequencies below 1 mHz. However, a growing number of deployments with broadband, highfidelity sensors to periods 120 s or longer means that the

higher-frequency normal modes, that sample shorterwavelength Earth structure, require networks of instru-

mentation on finer spatial scales. Although permanent

^{*}Corresponding author: Nicholas.harmon@whoi.edu

normal mode coverage gaps in the ocean are becoming filled.

Several studies reported observations of spheroidal normal modes on vertical components of very broadband OBS as the vertical components tend to be quieter than the horizontal components (Bécel et al., 2011; Deen et al., 2017; Laske, 2021). Normal modes were reported in data recorded by free fall instruments in the Lesser Antilles using Scripps-designed OBSs equipped with Nanometrics Trillium T-240 broadband seismometers (Bécel et al., 2011). The instruments recorded the M_w =8.1 April 1, 2007 Solomon Islands event, and lowfrequency modes were observed down to $_0S_6$ (f = 1.04 mHz). Another study, using the same type of OBSs in the Rhum-Rhum experiment in the Indian ocean, consistently recorded normal modes in Earth's Hum band between 2.49 - 4.5 mHz throughout the year-long deployment from 2012 to 2013 (Deen et al., 2017). Observation of these modes was possible after applying deglitching of electrical noise, caused by the leveling cycles of the seismometer, as well as tilt and compliance corrections (Bell et al., 2015; Crawford and Webb, 2000). In a recent study, Laske (2021) evaluated spheroidal normal mode signals from several large magnitude earthquakes recorded on OBSs deployed as part of the PLUME experiment near Hawaii (Wolfe et al., 2009), the NoMELT experiment in the central Pacific (Lin et al., 2016), and the ALBACORE (Bowden et al., 2016) and ADDOSS (Berger et al., 2016) arrays offshore of California. The Scrippsdesigned OBSs equipped with the T-240 seismometers were consistently successful at recording spheroidal modes on vertical components, with perhaps surprisingly high signal-to-noise (SNR) levels, although site effects, ocean currents, infragravity waves and/or isolated technical limitations at individual sites generated some variability in the performance. Where direct comparisons were available, however, land-based seismometers yielded substantially better low-frequency spectra than free-fall OBSs. For example, Laske (2021) documented that the land-based GSN observatory station Kipapa, Hawaii (KIP) recorded normal mode $_0S_3$ (f = 0.47) mHz) for the 28 March 2005 Sumatra-Andaman earthquake, but the 'best' PLUME OBSs recorded high-SNR modes only down to ${}_{0}S_{8}$ (1.41 mHz). Hence, it is appropriate to note that all these publications are a manifest that broadband sensors can record spheroidal normal modes, though with some caveats. First, corrections to the data often need to be applied to account for tilt and compliance noise due to the propagation of ocean infragravity waves. Second, the horizontal components needed for measuring toroidal normal modes are generally not useable, although the PLUME records yielded Love wave phase velocity curves for frequencies $f \ge 10$ mHz (Anarde and Laske, 2010).

In this paper we present observations of spheroidal normal modes from a broadband OBS array in the equatorial Mid-Atlantic deployed as part of the Passive-Imaging of the Lithosphere-Asthenosphere Boundary (PI-LAB) experiment and the Experiment to Unearth the Rheological Lithosphere-Asthenosphere Boundary (EURO-LAB) which consisted of 39 OBSs. The OBSs were co-located with 39 magnetotelluric instru-

ments deployed by the Central Atlantic Lithosphere-Asthenosphere Boundary (CA-LAB) experiment. There were also several active source components including the Trans-Atlantic I-Lab experiment (Mehouachi and Singh, 2018). The combined experiments were designed to use methodologies sensitive to a range of resolutions and sensitivities in a single study area beneath seafloor formed at the nearby slow spreading Mid-Atlantic Ridge to image the lithosphere-asthenosphere system and determine what makes a plate, "plate-like." These studies found that the lithosphere-asthenosphere boundary beneath the Atlantic is defined to first order by temperature, but that it is also dynamic and dictated by variations in melt generation and migration (Fischer et al., 2020; Harmon et al., 2018, 2020, 2021; Rychert et al., 2020, 2021; Wang et al., 2019, 2020; Saikia et al., 2021a,b). A number of other studies were possible with the data including, for instance, locating the source regions of infragravity waves (Bogiatzis et al., 2020), local seismicity work (Hicks et al., 2020; Leptokaropoulos et al., 2021, 2022; Schlaphorst et al., 2022), sediment constraints (Agius et al., 2018; Saikia et al., 2020), mantle transition zone imaging (Agius et al., 2021), and the work presented in this manuscript. In the experiment 24 OBSs were equipped with a Nanometrics T-240 broadband seismometers (Fig. 1), and 15 OBSs were equipped with a Nanometrics Trillium Compact wideband seismometers. The latter 15 OBS are not considered here. Of the 24 broadband OBSs, 15 provided useable data for the purposes of this paper. We present a new means for correcting tilt through a simple rotation rather than the commonly utilized spectral transfer function method (Deen et al., 2017; Crawford and Webb, 2000). We show that in some cases it substantially improves SNR ratios at low frequencies (f < 3 mHz). The rotation also conserves the energy on the seismograms without introducing artefacts to the vertical component that can be caused by band-limited spectral multiplication. We also make measurements of frequency shifts of the spheroidal modes and demonstrate that OBS records can be used to contribute to global data sets for improving global estimates of 3-D structure.

2 Methods

We use three component seismogram recordings and Cox-Webb differential pressure gauge (DPG) records (Cox et al., 1984) from Scripps-designed broadband OBSs that are equipped with Nanometrics T-240 seismometers from two OBS pools, Scripps Institution of Oceanography (SIO) and Institut de Physique du Globe de Paris (IPGP). The IPGP equipment are an older generation of the SIO design and have an electrical glitch approximately every hour caused by the leveling schedule. The SIO equipment have a variable leveling schedule, approximately every week for the majority of the deployment. Station names beginning with "I" are from the IPGP pool and those beginning with "S" are from the Scripps pool.

The time series are from two M_w =7.9 earthquakes located in Papua New Guinea on December 17, 2016 at 10:51 GMT at 153.52°E, 4.5049°S and 94.5 km depth and

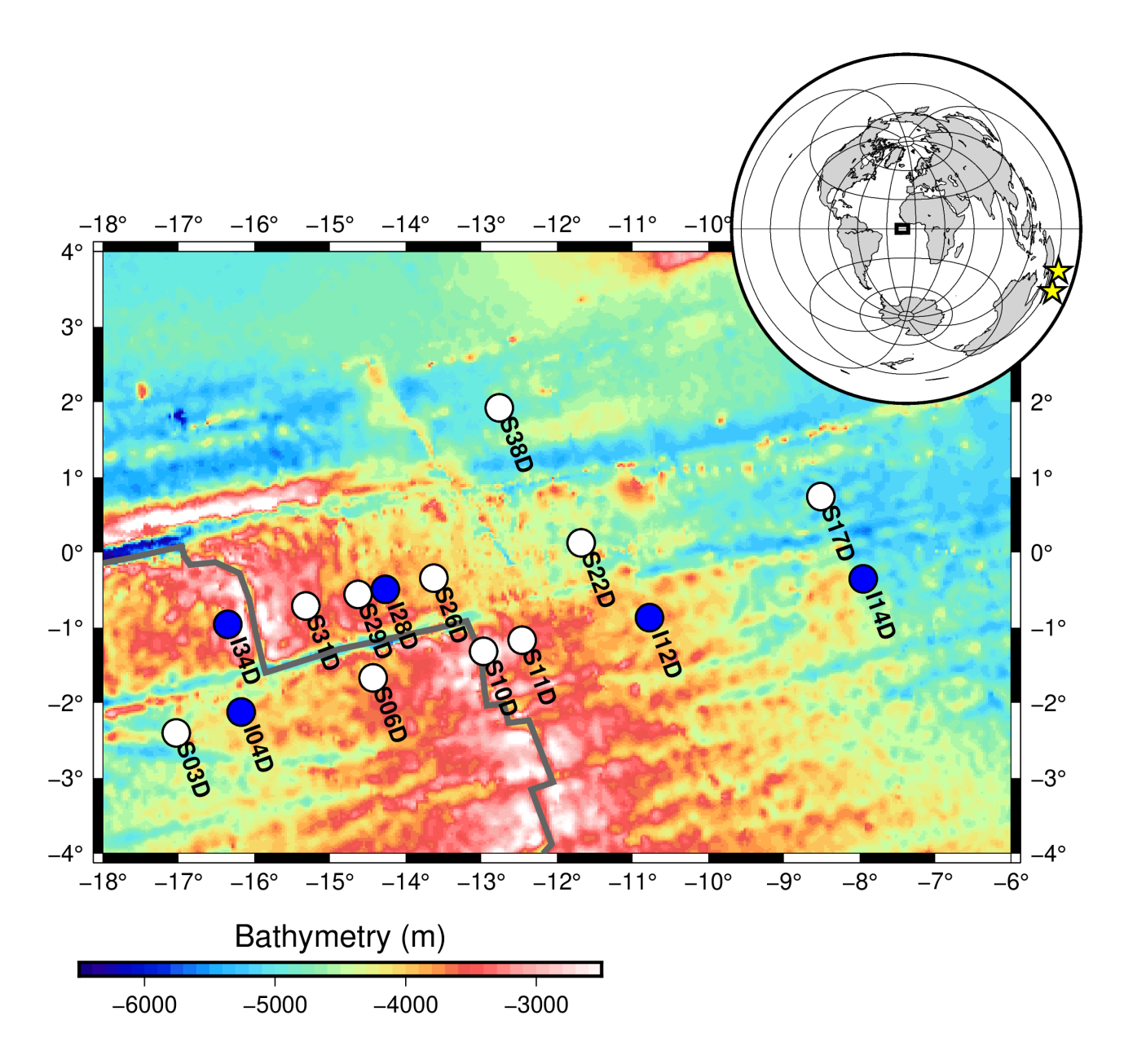


Figure 1 Bathymetry map of the PI-LAB study region. Locations of the T-240 seismometers are shown as circles, white for Scripps Institution of Oceanography instruments, blue for Institut du Physique du Globe instruments. Stations names are as labeled. Grey line shows the location of the Mid-Atlantic Ridge system. Inset map shows the location of the PI-LAB study area (black box) and the location of earthquakes used in this study (yellow stars).

on January 22, 2017 03:07 GMT at $155.1718^{\circ}E$, $6.2463^{\circ}S$ and 135 km depth (Fig. 1 inset). We use time series that begin 5000 s before the event origin time and last for two days after the origin time.

We pre-process the IPGP data to remove the electrical leveling glitch using a comb filter and following a similar method to Deen et al. (2017). We first identify a target glitch waveform during a quiet period (Figs. 2, 3). This waveform is then correlated with the entire waveform to identify the time range of each glitch in the time series. We search in all time periods where we expect the glitch to occur, i.e., every hour. For each glitch time range we solve for the best fitting amplitude of the target glitch waveform and subtract it from the waveform. A detailed example of the deglitching is showing in Figure 3.

We determine the tilt of the vertical component for all stations. We assume the tilt is static for the duration of the time window of our normal mode analysis. Even though tilt may change through time, especially after a re-leveling cycle of the OBS, our static tilt assumption is likely valid. Our analysis time periods are chosen to roughly fall in between leveling cycles to avoid those time periods. Therefore, the resulting tilt corrections are typically consistent through time for each instrument (Tables 1, 2). We bandpass filter the raw data between 0.1 – 10 mHz for one day of quiescent data approximately two days after the main event. We then search for the best-fitting tilt from vertical and azimuthal rotation angle, i.e., azimuthal direction of tilt, that minimizes the root-mean-square of the rotated vertical com-

ponent. Specifically, we apply an azimuthal rotation for the BH1 and BH2 horizontal components into a radial (in the azimuthal direction of the tilt) and transverse (perpendicular to the azimuthal direction of the tilt) component for a potential tilt direction. No information about the true orientation of the instrument's horizontal components is required. We then apply a vertical - radial component rotation to minimize the energy on the rotated vertical component. Once these angles are determined the rotation is applied to the raw data to determine the tilt corrected data. We then estimate a compliance correction to the vertical component using the spectral transfer function method between the differential pressure gauge record (DPG) and the tilt corrected vertical component. We use the same day-long time series (Crawford and Webb, 2000) used in the tilt estimations. The transfer function is used to estimate a predicted vertical component from the DPG record, which is then subtracted from the tilt corrected vertical component. We apply the compliance correction in the frequency band where the coherence between the pressure and tilt corrected vertical component is > 0.8. The instrument response is then removed, and the velocity seismograms are differentiated to acceleration. Acceleration records are used as opposed to velocity or displacement for two reasons: 1) the community's normal mode theory is based on acceleration and 2) the amplitudes at ultra-low frequencies are suppressed, i.e., those where we usually see increased noise levels because they are beyond the frequency roll-off of almost all seismometers.

We then estimate the normal mode spectra from the vertical components of the events. First, we apply a 4th order Butterworth filter with a 0.3 mHz high pass corner frequency. We choose a time window that begins 5000 s before the origin time and ends two days after the origin time. This window is optimal because it includes as many stations as possible, while avoiding the variable leveling cycles of the Scripps instruments. We then estimate the spectra using a single Slepian taper (NW=2, with 1 taper used). This is similar to using a single Hanning window, which has been successfully used in previous studies (e.g. Masters and Widmer, 1995). We compare the spectra of the resulting data, i.e., with the instrument response, glitch, tilt, and compliance corrections applied, to the spectra of data that have had just the instrument response removed and a high pass filter applied. We will refer to the first case as "corrected," and the second case as "uncorrected."

To assess the effects of the seismogram corrections on normal mode observables, we measure normal mode peak frequencies, at each of the PI-LAB stations, for each weakly coupled mode between $_0S_9$ and $_0S_{40}$. The procedure is interactive, where we fit a decaying cosine function to the corresponding spectral peak in a least-squares fitting process. To compute the mode spectrum for a specific mode, we use an optimal window length corresponding to Q-cycles of a mode (Dahlen, 1982), the time within which the mode decays to 1/e of its initial amplitude. A Hanning taper is applied. A successful fit and removal of the cosine function leads to a residual spectrum with a 'clean hole'

left in the spectrum that allows the analyst to assess whether or not a fit was successful or if the measurement has to be discarded. In the latter case, the synthetic mode has a realistic frequency but unrealistic attenuation, and the residual spectrum has remaining spectral peaks adjacent to the synthetic mode. Reasons for unsuccessful fits include noisy signals and the presence of other modes. This mode measurement method was used by Smith and Masters (1989) to explore longwavelength 3-D structure in the mantle. The underlying principle here follows the assumption that a mode frequency shift that is measured at a recording station is caused by structure only along the source-receiver great circle, and is represented by structure at the two poles of that great circle (Backus, 1964). Even though an isolated mode ₀S₁ is sensitive to structure of harmonic degree up to s=2l, asymptotic peak shift theory is a valid approximation only as long as s « l. A second caveat to this theory is that second-order effects introduce a 'jitter' in the frequency measurements that depends on epicentral distance (Dahlen and Tromp, 1998). For these reasons, asymptotic peak shift theory and associated work fell out of favor and is currently not typically pursued. However, the interactive measurement technique is suitable for initial quality assessment and to explore the internal consistency of normal mode data measured on PI-LAB OBS records. Therefore, we apply it here.

3 Results

We present time domain vertical component waveforms for the 2016 event for three representative stations, I28D, S11D and S17D to illustrate the data quality and the effects of the deglitching and tilt corrections. We present I28D to illustrate the leveling glitches. S11D is a quiet station with little to no tilt. S17D is a station that has a high tilt, 0.89°. The noise levels are visibly low for the vertical component for all three stations prior to the event in the uncorrected data (Fig. 2, black lines) and in the corrected data (Fig. 2, orange lines). In addition, the Rayleigh wave orbits (Fig. 2, R1 - 9) are visible on S11D, which is a particularly quiet station. The Rayleigh wave orbits are less visible on S17D in the uncorrected data as there are several transient high noise time periods visible, an example of which is indicated by the blue arrow above the record. In the corrected data, these transients are substantially reduced, in particular near the blue arrow. In general, the corrections have a minimal impact on the amplitude of the observed phases, reducing the amplitude within R1 by < 10% for S17D, and by 3 – 4% for S11D. For I28D, two of the leveling glitches are indicated by cyan arrows above the traces, although several others are visible in the record. The effect of the corrections greatly reduces the amplitude of the glitches in comparison to those of the uncorrected data (orange vs. black lines, respectively), although the tilt noise is relatively low for this station, and there are no noise transients visible away from the glitches as in S17D. Greater deglitching detail is shown in Figure 3. Figure 3 highlights the contamination of the glitches on measurements of the modes. Many of the glitch harmonics (black stars) occur at frequen-

Station	Tilt Azimuth (Relative to North) °	Tilt Angle From Vertical °
S03D	321.87	0.48
S06D	107.25	0.40
S10D	76.91	0.18
S11D	308.40	0.13
S17D	288.97	0.89
S22D	154.27	0.17
S26D	118.11	0.18
S29D	245.43	0.16
S31D	225.19	0.23
S38D	94.07	0.09
104D	42.93	0.07
I12D	34.08	0.02
I14D	54.32	0.09
128D	46.52	0.05
134D	61.07	0.07

Table 1 Tilt Corrections for Mw = 7.9, 2016-12-17T10:51:10, Papua New Guinea

Station	Tilt Azimuth (Relative to North) °	Tilt Angle From Vertical °
S03D	311.90	0.65
S06D	115.30	0.46
S10D	77.46	0.19
S11D	298.18	0.09
S17D	288.80	0.91
S22D	154.90	0.14
S26D	119.80	0.20
S29D	243.89	0.19
S31D	224.71	0.19
S38D	92.87	0.11
104D	34.05	0.07
I12D	41.94	0.02
114D	54.26	0.09
128D	46.01	0.05
134D	65.93	0.07

Table 2 Tilt Corrections for Mw = 7.9, 2017-01-22T04:30:22, Papua New Guinea

cies near fundamental-mode frequencies (thin vertical black lines). The noise levels after deglitching also increase at frequency < 2 mHz, likely due to imperfect glitch removal. Although a correction for compliance due to infragravity waves using the pressure component (Webb and Crawford, 1999) is applied to all of the data, its magnitude is very small for the time period of the two events.

We show the effect of the tilt corrections on the spectra for station S17D for the 2016 event in Figure 4. The spectra from uncorrected data are shown in black and the tilt corrected waveforms are in orange. Spectral peaks associated with most of the zero order modes, with global average frequencies (Masters and Widmer, 1995), indicated by thin vertical lines, can be seen in the uncorrected and corrected data above 2.75 mHz. For the uncorrected spectra the peaks are clearly visible as low as 1.75 mHz, although the spectra have a high noise background, around 0.5x10⁻¹³ m/s²/Hz, at frequencies lower than 2.75 mHz. This high noise background obscures many of the smaller peaks associated with modes between ${}_{0}S_{10}$ to ${}_{0}S_{19}$. The corrected spectra have a much lower noise background in general, particularly below 2.75 mHz with a noise floor of $\sim 1 \times 10^{-16}$ m/s²/Hz (orange line, Fig. 4). Peaks associated with ${}_{0}S_{6}$ to ${}_{0}S_{19}$ and other modes are visible, standing clearly out from the background. In the corrected records, the amplitudes of some of the modes above $_0S_{19}$ are reduced relative to the uncorrected spectra, by up to 28% in some cases ($_0S_{19}$). In other words, the correction has minimized the background noise, which is a similar order of magnitude in the 1.5–2.5 mHz band to the modes, in the instrument uncorrected spectra (black lines).

We also compare the results of the rotational tilt correction and spectral compliance correction presented here to the results using the spectral tilt and compliance correction method (Bell et al., 2015; Crawford and Webb, 2000) for station S17D in Figure 4b (cyan line). We use a variation of the method that employs a grid search of tilt azimuth for the highest average coherence in the frequency band of interest between a test radial component for the direction of tilt and the vertical (Bell et al., 2015). It shows a similar improvement to the rotational tilt correction presented here above 1 mHz. However, the spectral method performs worse at reducing noise at < 1 mHz, likely due to lower coherence in the lowest frequencies. The same is true at other stations with less tilt (Figs. S1 and S2).

The corrected normal mode spectra are shown for all useable stations from the array for the 2016 event

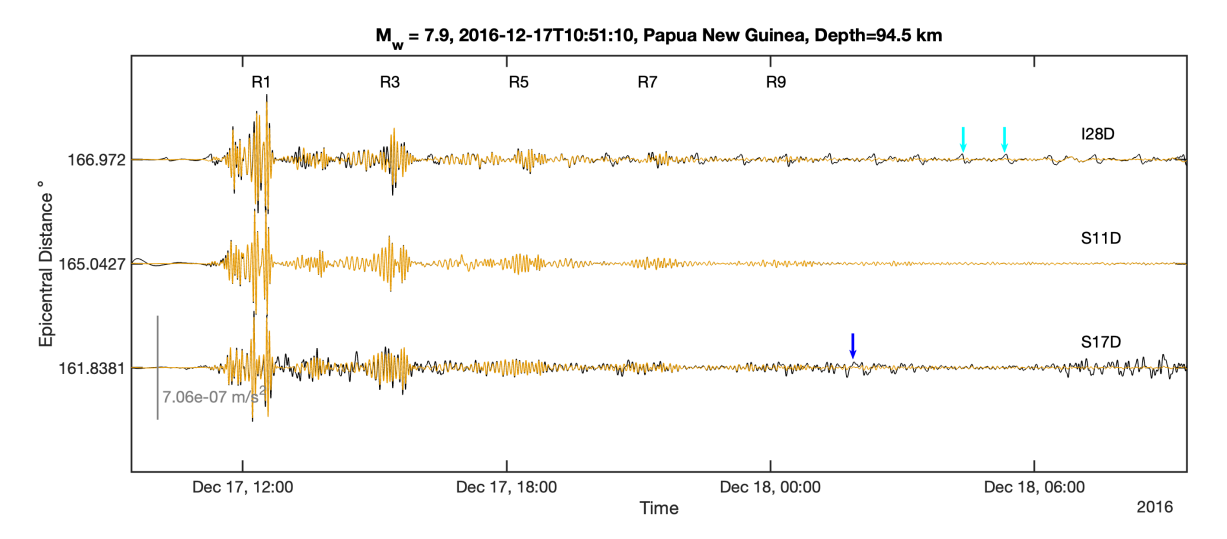


Figure 2 Example acceleration seismograms from the 2016 event used in this study. The seismograms are plotted as a function of epicentral distance in degrees, indicated on the y-axis. Scale bar for the amplitude of the seismograms is given (grey vertical line). Black seismograms show uncorrected seismograms (only instrument response removed and high pass filter applied), while orange lines show corrected seismograms. The seismograms have been filtered between 0.3 – 10.0 mHz. Station names are given above each trace. Theoretically predicted minor arc (odd) R1-R9 arrivals are indicated. Major arc (even) arrivals are not indicated as they arrive shortly before subsequent minor arc arrivals due to the large epicentral distance. Cyan arrows indicate two example leveling glitches on the IPGP stations. Blue arrow indicates a region where tilt correction removes a substantial amount of noise.

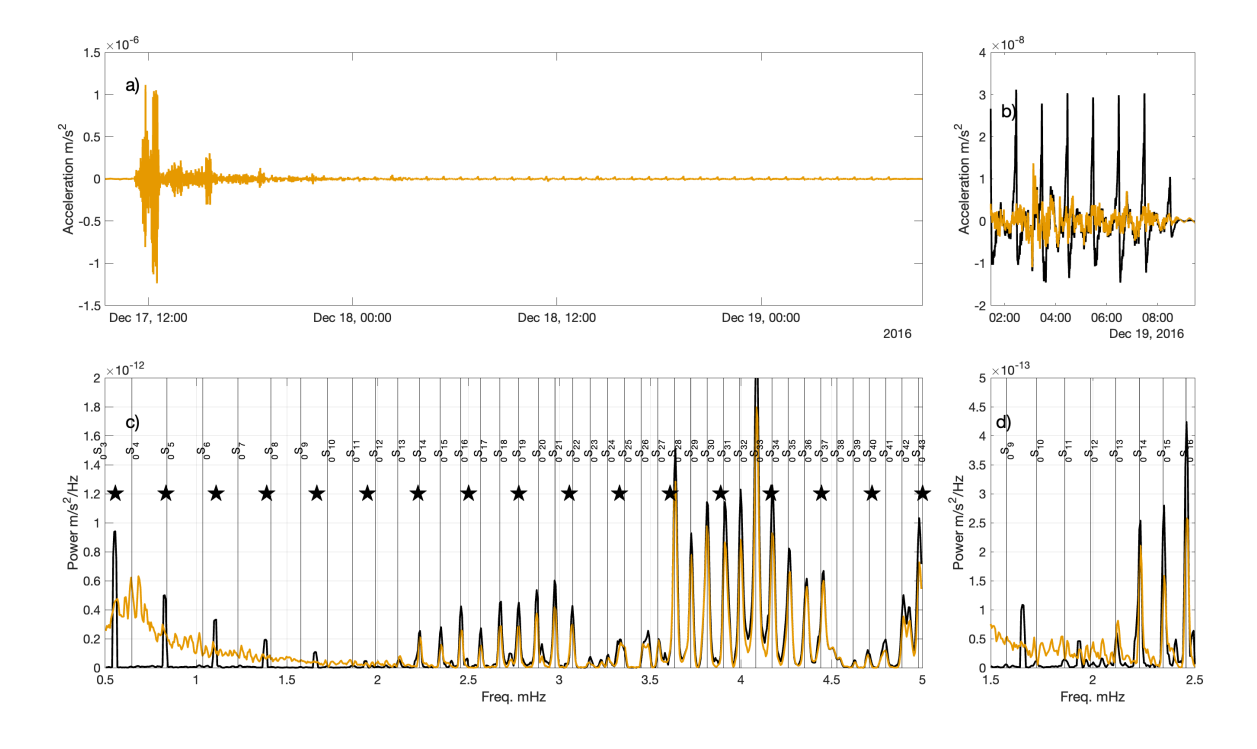


Figure 3 Leveling glitch correction for station I34D. Black lines show the uncorrected data and orange lines show the corrected data. a) The time series over a 48 hour period and b) a zoom of an 8 hour period are shown. c) The spectra from 0.5-5.0 mHz and d) a zoom from 1.5-2.5 mHz are shown. Black stars indicate the location of hourly harmonics from the leveling glitch. Global average fundamental mode frequencies are shown by thin vertical lines, and modes are labeled at amplitude = 1.5 (Masters and Widmer, 1995).

(Fig. 5) and the 2017 event (Fig. 6). The tilt corrections applied to each station for each event are given in Tables 1 and 2, respectively. The records show very consistent peaks for the zero order spheroidal modes, especially above $_0S_{11}$ for the 2016 event, while for the 2017 event peaks are consistently observed above $_0S_{14}$.

In the 2016 event a strong beating pattern is observed in all the records that becomes broader and shifts toward higher frequencies with increasing epicentral distance. This is the predicted behavior of the amplitudes of the zero order spherical harmonics at a given distance from the source to its pole (Laske and Widmer-

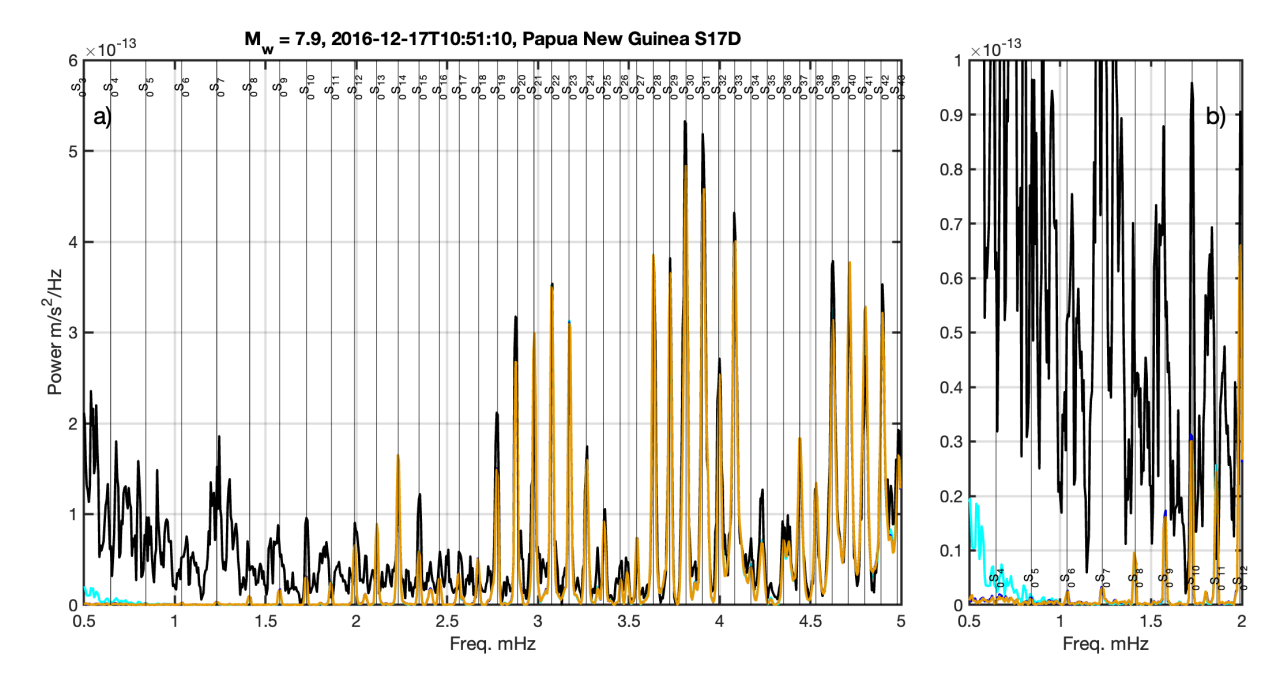


Figure 4 Example spectra after the application of tilt and compliance corrections for the 2016 event to station S17D which had a tilt of 0.89° . a) The spectra from 0.5-5.0 mHz and b) a zoom of 0.5-2.0 mHz are shown. In both panels, the black lines show the spectra of the uncorrected data. The blue line (for instance, visible in b) near $_0S_4$ behind the orange line) shows the tilt response corrected data. The orange line shows the tilt and compliance corrected data. The blue and orange lines are nearly identical, with the largest difference (7%) observed at $_0S_9$. The cyan line shows the result from the spectral tilt correction (Bell et al., 2015; Crawford and Webb, 2000). Global average fundamental mode frequencies are shown by thin vertical lines, and modes are labeled (Masters and Widmer, 1995)

Schnidrig, 2015). In other words, each station spatially samples the modes slightly differently depending on its epicentral distance to the event because adjacent modes with similar wavelengths come into and out of phase with each other. This beating pattern is less visible in the 2017 event. The lowest zero order mode observable in the data set is ₀S₄, which is observed at S29D for the 2016 event, and ₀S₅, which is observed at several stations for the 2017 event. In detail several other modes are visible in the spectra as smaller peaks adjacent to the zero order modes. In general, the IPGP stations are noisier by an order of magnitude or more, especially at frequencies below 2 mHz. This is mostly due to imperfect removal of the leveling glitches, which have strong harmonics in this frequency range (harmonic locations indicated by black stars, Fig. 3). IPGP records above 2 mHz are comparable to the SIO stations.

All the measurements for the array for modes $_0S_{14}$ and $_0S_{23}$ are displayed in Figure 7. We observe a surprisingly complex pattern of frequency shifts across the network, and hypothesize based on modelling work that long-wavelength 3-D structure can cause such variations. For this comparison, we compute normal mode structure coefficients, c_s^t for mantle model S20RTS (Ritsema et al., 1999) but include harmonic degrees only up to s = 12 to compute predicted peak shifts. Even then, the patterns in the theoretical peak shifts are quite complex, and exhibit similarities with our observed peak shifts. Note that the frequency shifts are plotted at the stations, while using asymptotic peak shift theory implies that associated structural variation would be located at the two

source-receiver great circle poles, which are broadly located in northern Russia (about 65°N/75°E) and in the Southern Ocean east of the Antarctic peninsula (about 65°S/105°W).

Measurements for other modes are not as internally consistent, but we can still assess overall average mode frequency observations across the array. These are shown in Figure 8. We omit measurements for modes that are strongly coupled to toroidal modes, $_0S_{11}$, $_0S_{18}$ and $_0S_{19}$. We take two sets of measurements, one on the raw seismic records, and one on the rotation and compliance corrected seismograms. We find that the correction does not change overall averages to a significant level. In fact, measurements for modes of angular order 1 < 20 may exhibit smaller standard deviations, indicating a more internally consistent set of measurements.

4 Discussion

The deglitching we perform on the IPGP instruments is effective. Without the correction there are strong harmonics in the data that interfere with the normal modes, making clear analysis difficult (black lines, Fig. 3). After the correction the leveling glitch harmonics are greatly reduced in the spectra, and the normal modes stand out better (orange lines, Fig. 3). We observe small artifacts in our time domain waveform due to the leveling glitch removal, which may explain why noise remains relatively high at the lowest frequencies. The IPGP station noise levels are higher than the SIO station noise levels below 2 mHz even after applying the

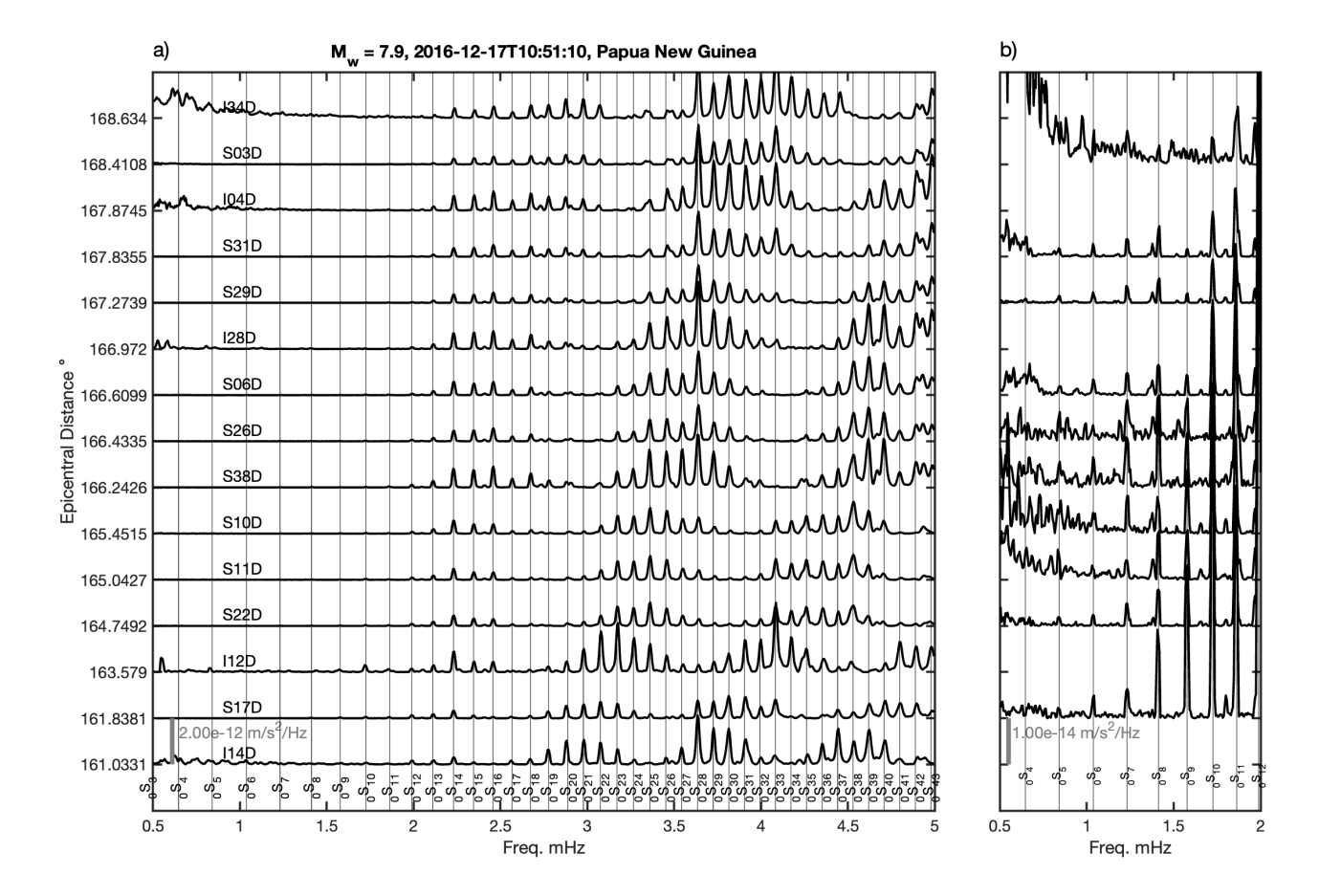


Figure 5 Compiled spectra for all useable stations for the 2016 event. a) The spectra as a function of epicentral distance indicated on the y-axis over the 0.5-5.0 mHz range and b) a zoom into the 0.5-2.0 mHz range are shown. Stations are labeled and a scale bar (grey vertical line) is given in each panel. Global average fundamental mode frequencies are shown by thin vertical lines, and the modes are labeled (Masters and Widmer, 1995). In panel b) stations with high noise are excluded from the plot.

deglitching correction (Fig. 5 and 6). Our findings are similar to previous work (Deen et al., 2017), which found similar success in removing the leveling glitches. Our result suggests that data from earlier deployments with the same leveling glitches might be used for future normal mode studies at least above 2 mHz.

The corrections applied here allow us to observe modes at a similar range observed in previous OBS data, but they also improve the number of stations that observe the lowest modes. We observe spheroidal modes down to ₀S₄ or ₀S₅ depending on the instrument. This is similar to reports from deployments using similar instrumentation, which observe spheroidal modes down to ₀S₄ (Bécel et al., 2011; Laske, 2021). Our quietest station (S29D) yields the widest frequency band of observation and is comparable to the performance of the same type of instrument in numerous other ocean bottom deployments. Given the large number of usable stations and the routine observations of spheroidal modes to 0S9 at 9 out of 15 stations for the 2016 event and 10 out of 15 stations for the 2017, we are able to make estimates of frequency shifts relative to 1-D reference mode frequencies (Masters and Widmer, 1995) over $_0S_9 - _0S_{40}$. Although the lowest modes observed are similar to previous work, the corrections allow us to observe lower modes at several stations that would otherwise not have been possible, which we describe in the next three paragraphs.

The simple rotation to correct for tilt presented here offers an effective alternative to the commonly used spectral tilt correction (Crawford and Webb, 2000) for reducing long period noise. The advantage of this method is that it is conserves energy across all three components and across all frequencies as it rotates the energy between the components. The spectral domain tilt correction is typically only applied in a frequency band where the coherence is high between the vertical and horizontal components, and so may only improve SNR in this band. The rotation tilt correction provides the greatest noise reduction below 3 – 3.5 mHz in the example shown in Figure 3, in which the noise floor is reduced by 2 - 3 orders of magnitude. Similar performance below 3 mHz is observed at several other stations. Below 1 mHz, the rotational method outperforms the spectral tilt correction. Tilt angles from the vertical component estimated for the stations used here range from 0.91° to 0.02° for the two events. Unfortunately, the tilt correction is not successful at enhancing SNR on

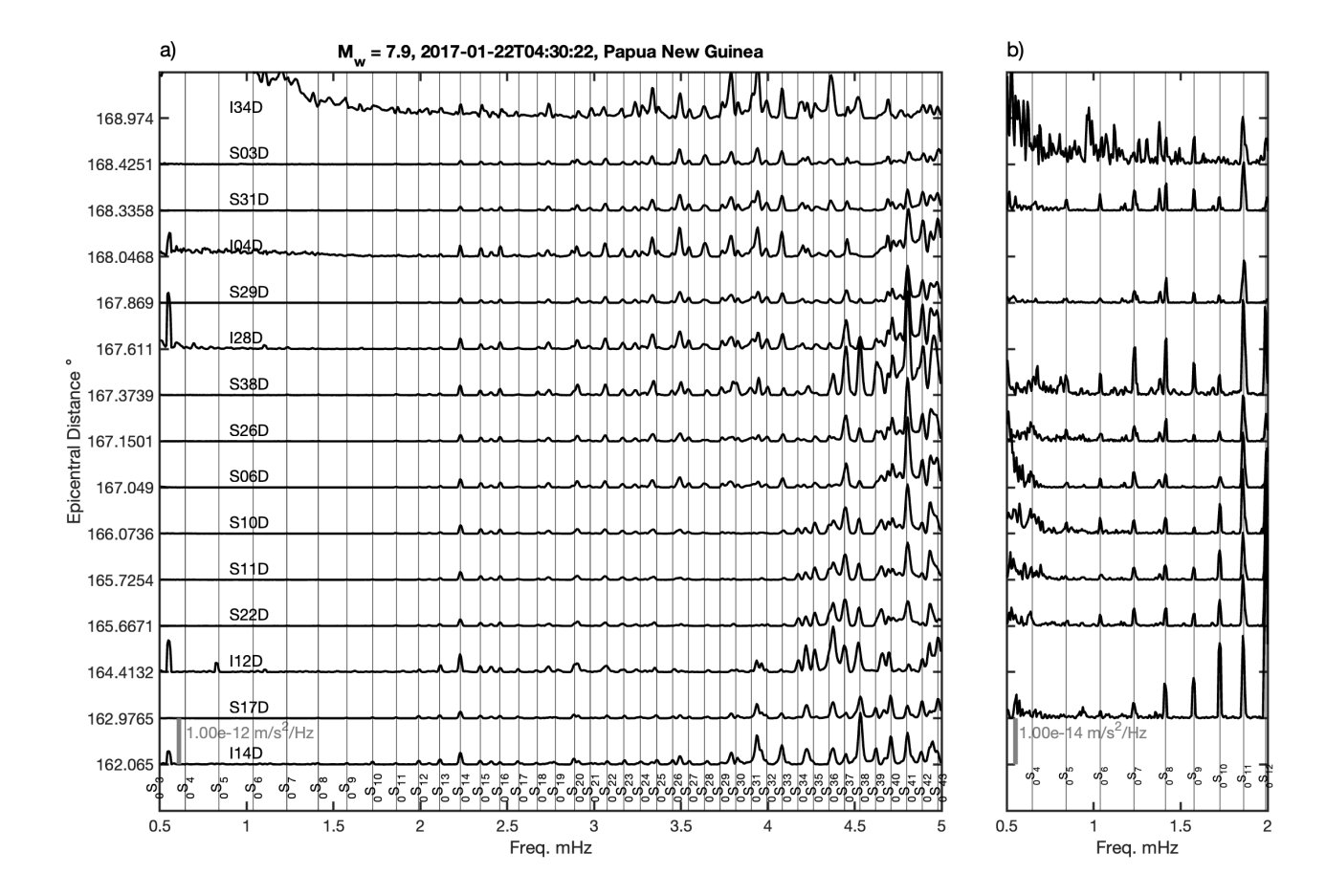


Figure 6 Compiled spectra for all useable stations for the 2017 event. a) The spectra as a function of epicentral distance are indicated on the y-axis over the 0.5-5.0 mHz range and b) a zoom into the 0.5-2.0 mHz range are shown. Stations are labelled and an amplitude scale bar (grey vertical line) is given in each panel. Global average fundamental mode frequencies are shown by thin vertical lines, and modes are labelled (Masters and Widmer, 1995). In panel b) stations with high noise are excluded from the plot.

the horizontal components for these events. However, future deployments may yield toroidal modes in quieter settings. The pressure correction that is required is very small and, in most cases, has little effect on the SNR of the normal mode spectra. The small correction is likely due to the low infragravity wave conditions for most of December 2016 and January 2017 (Bogiatzis et al., 2020).

The leveling glitch correction applied here shows some improvement in comparison to previous work. One-hour harmonics were deleted in the spectra shown in Bécel et al. (2011) from the leveling glitches, effectively eliminating information at the frequency of the glitches. The corrections we use here greatly reduce these harmonics without deleting sections of the data. Using the correction approach of this work the glitch harmonics, i.e., the peaks in between the 1-D reference mode frequencies (Harmon et al., 2021) (black lines at < 2 mHz, Fig. 3) are not visible in the orange lines, but our spectra maintain information at these frequencies. The performance of our method is similar to the performance reported in Deen et al. (2017). These corrections are needed to measure normal modes using data with glitch harmonics.

The tilt correction lowers the noise floor at low fre-

quencies, effectively allowing mode observations and measurements. The noise floor at < 2.75 mHz is high in previous work (Bécel et al., 2011; Laske, 2021), likely due to tilt, increasing by up to 20 dB below 1 mHz. This high noise floor below 2.75 mHz is visible in other deployments as well, for example several stations (e.g. PL05, PL35) from the PLUME experiment (Laske, 2021). The tilt correction effectively removes similar noise in our study (black vs. orange lines in Fig. 4), again facilitating observation and measurement of the modes at frequencies below 2.75 mHz. This tilt noise likely exists in data from other previous experiments. Therefore, mode observation and measurement can can likely be improved for this previous data.

Comparison of our mode frequency shifts to the 1-D reference mode frequencies (Masters and Widmer, 1995) highlights important deviations that reflect unaccounted for Earth structure. In comparison to the 1-D reference mode frequencies we find deviations that increase with increasing angular order l (Masters and Widmer, 1995). This indicates structural deviation from the underlying 1-D reference model for our sampled source-receiver great circles. These deviations are likely related to structural heterogeneity in the up-

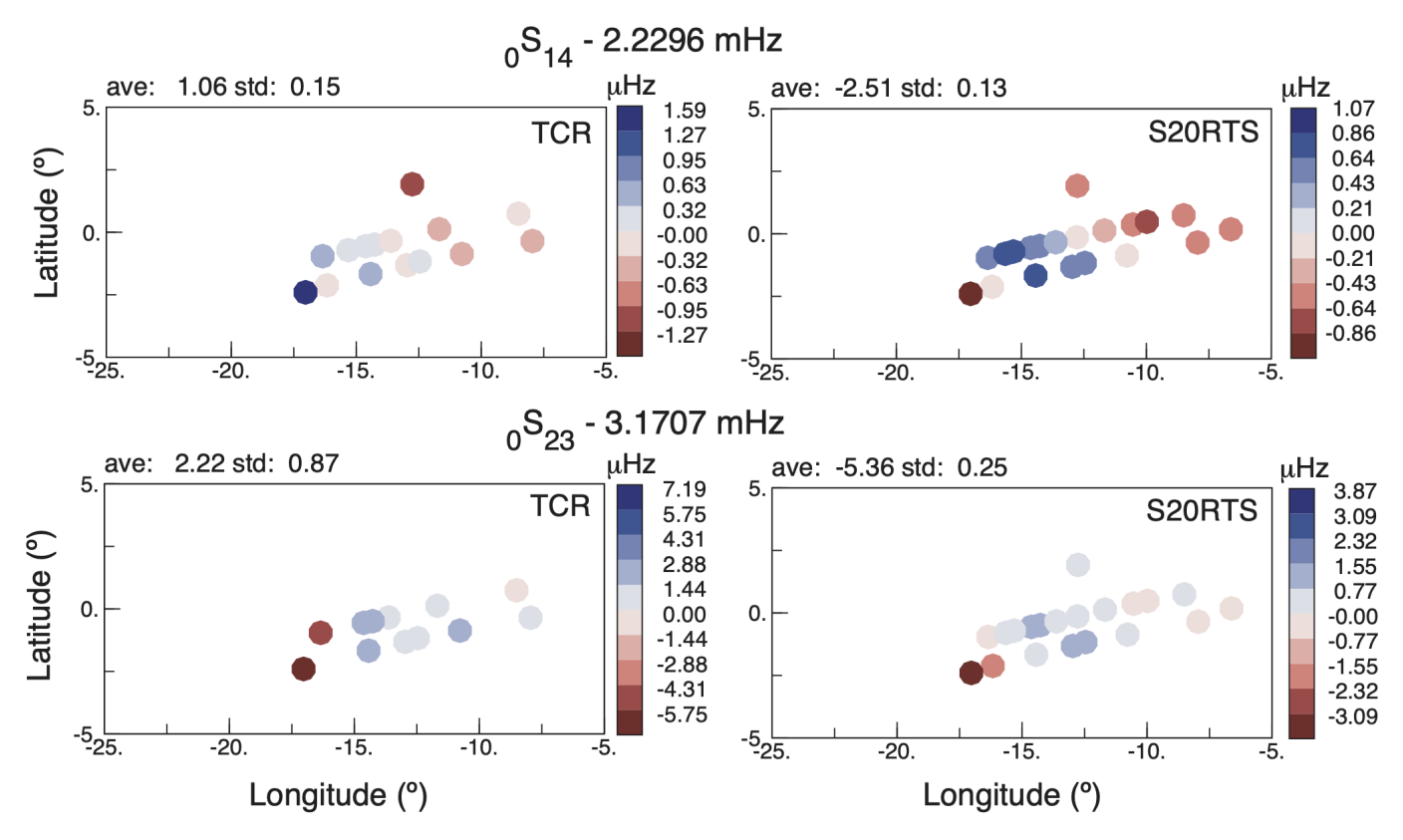


Figure 7 PI-LAB peak shift measurements for modes ${}_{0}S^{14}$ and ${}_{0}S^{23}$ (left column, tilt, compliance, and rotation correction) and corresponding predictions for model S20RTS (Ritsema et al., 1999) (right column) relative to the global 1-D reference mode frequencies of Masters and Widmer (1995). Earth's hydrostatic ellipticity has not been considered in the predictions for model S20RTS. The averages of the measurements were removed before plotting (upper left of panels). Measurements are plotted at the respective PI-LAB station locations. The titles identify the mode names and the average mode frequencies from Masters and Widmer (1995).

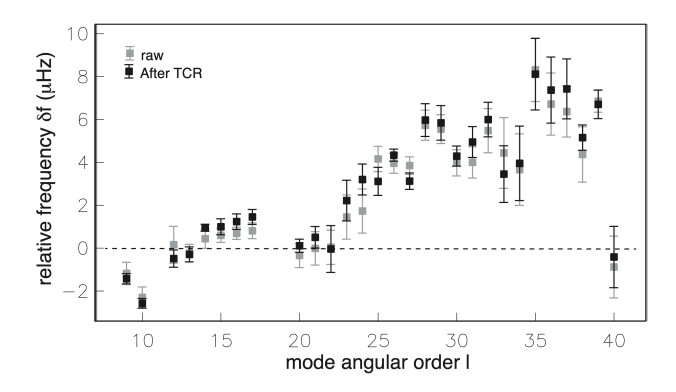


Figure 8 Averages of PI-LAB mode frequencies relative to those of Masters and Widmer (1995). Grey: raw measurements; black: after tilt, compliance and rotation correction (TCR). Error bars denote the standard deviation in the measurements taken across the network.

per mantle rather than in the lower mantle as modes around $_0\mathrm{S}_{30}$ reach only into the mantle transition zone, but not beyond.

Ultimately, we want to compare our mode frequency shift results with 3-D global velocity model predictions (Masters et al., 2000; Ritsema et al., 1999), for consistency. The predictions for 3-D global velocity model S20RTS are shown in Figure 9 (blue diamonds). Inspection of our results compared to 3-D model predic-

tions indicates a discrepancy of a DC shift of ~5 μ Hz. The discrepancy can be explained by the need to account for hydrostatic ellipticity in the predictions. Ellipticity has a significant effect that increases with angular order l, when compared to the 1-D reference mode frequencies (brown diamonds in comparison to black dashed line, Fig. 9) (Masters and Widmer, 1995). The predicted frequency shifts for S20RTS without ellipticity (blue diamonds) are smaller and mostly negative than those including the ellipticity correction (black squares). However, the two have very similar shapes given the nearly linear shape of the ellipticity correction. We also compare PREM (Dziewonski and Anderson, 1981) to our 1-D reference mode frequencies (Masters and Widmer, 1995) and find relatively small deviations (grey diamonds vs. black dashed line, Fig. 9).

Our results compare favorably with two global models: S20RTS (Ritsema et al., 1999), including the ellipticity correction, and SB4L18 (Masters et al., 2000), including the ellipticity correction in the range $14 \le l \le 37$. This suggests that we are recovering information about real Earth structure (Fig. 10). At lower angular orders, $9 \le l \le 14$, the agreement between our result and the two 3-D models is poor, suggesting our observations may not be as reliable for determining Earth structure for $l \le 14$. We find good general agreement between our model, S20RTS, and SB4L18 at $15 \le l \le 20$. From $21 \le l \le 32$ our result agrees better with predictions from S20RTS, al-

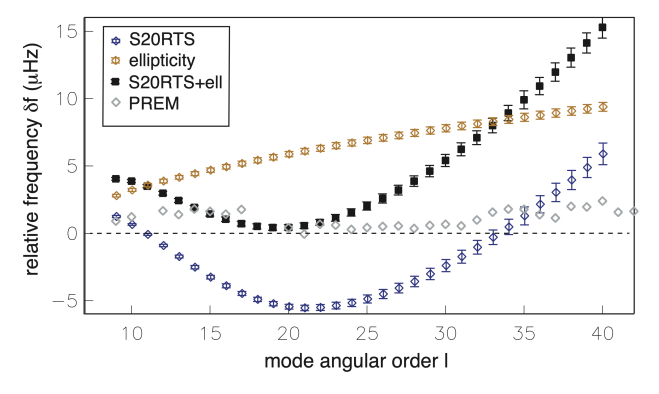


Figure 9 Averages of predicted mode peak shifts relative to those of Masters and Widmer (1995). Predicted mode frequencies are computed at all PI-LAB stations before averaging. We present a 3-D model S20RTS (blue diamonds) (Ritsema et al., 1999), Earth's hydrostatic ellipticity (orange diamonds), and the sum of the two (S20RTS+ell, black squares). Grey symbols mark frequency differences to Masters and Widmer (1995) computed for PREM (Dziewonski and Anderson, 1981) as published in Masters and Widmer (1995). The sum of PREM and S20RTS+ell is similar in magnitude and shape to the observations in Figure 8 and 10, indicating the need for the ellipticity correction.

though not consistently within error. From $33 \le l \le 37$ we find better agreement between our result and the predictions from SB4L18, typically within error. At l > 37, the differences between our result and the predictions from the 3-D models are large, suggesting that our result does not represent real Earth structure. The small but significant variations found between our observations and the two global models at $21 \le l \le 32$ indicates that incorporating information from OBS arrays such as ours into global normal mode inversions might improve our knowledge of Earth structure.

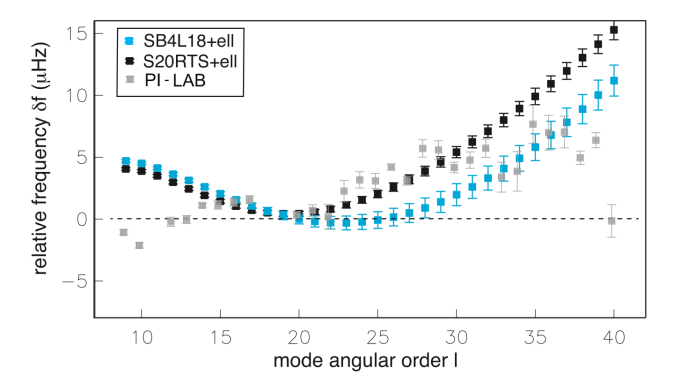


Figure 10 Averages of predicted mode peak shifts relative to those of Masters and Widmer (1995). These are shown for S20RTS (black symbols) (Ritsema et al., 1999) and SB4L18 (blue symbols) (Masters et al., 2000) both with Earth's hydrostatic ellipticity included (+ell). Grey symbols mark observations from PI-LAB shown in Figure 8 from the corrected data.

5 Conclusion

Broadband OBS can help to deepen our understanding of the interior of the Earth via normal mode observations by filling in the current gaps in global station coverage. We provide a new tilt correction technique using a simple rotation to improve observations at low frequencies that will be useful for recovering lower modes at additional stations as well as for other types of seismic observations. We present some of the first measurements of frequency shifts from a broadband ocean bottom seismic array, that could be combined with other global observations to invert for threedimensional Earth structure. Very broadband OBS are more expensive than more band limited instruments. However, installing very broadband instruments is preferable given that the data can be corrected to measure normal modes, filling in gaps in global observations, and improving constraints on Earth structures. This is especially true given the expense, time, effort, and logistical challenges involved in any seagoing expedition.

Acknowledgments

We thank the captain and crew of the R/V Marcus Langseth and the RRS Discovery and also the scientific technicians of the Scripps, Lamont Doherty and INSU pools. C.A.R. and N.H. were funded by the Natural Environment Research Council (NE/M003507/1) (PI-LAB) and the European Research Council (GA 638665) (EURO-LAB). G. L. was funded by NSF grant OCE1830959. We used data from the XS network (https://doi.org/10.7914/SN/XS_2016) (Rychert et al., 2016).

Data Availability

Data is archived in the IRIS DMC and will be restricted until funding on EURO-LAB ends. Rotation code is available with this publication in the supplemental material and at https://doi.org/10.5258/SOTON/D2394.

References

Agius, M., Harmon, N., Rychert, C., Tharimena, S., and Kendall, J. Sediment Characterization at the Equatorial Mid-Atlantic Ridge From P-to-S Teleseismic Phase Conversions Recorded on the PILAB Experiment. *Geophysical Research Letters*, 45, 2018. doi: 10.1029/2018GL080565.

Agius, M., Rychert, C., Harmon, N., Tharimena, S., and Kendall, J. A thin mantle transition zone beneath the equatorial Mid-Atlantic Ridge. *Nature*, 589(7843):562–566, 2021. doi: 10.1038/s41586-020-03139-x.

Anarde, K. and Laske, G. A Joint Rayleigh and Love Wave Analysis for the Hawaiian PLUME. In *Project AGU Fall Meeting*, San Francisco, 2010.

Backus, G. Geographical interpretation of measurements of average phase velocities of surface waves over great circular and great semi-circular paths. *Bull. Seis. Soc. Am*, 54(2):571–610, 1964. doi: 10.1785/bssa0540020571.

Bell, S., Forsyth, D., and Ruan, Y. Removing Noise from the Vertical Component Records of Ocean-Bottom Seismometers: Results

- from Year One of the Cascadia Initiative. *Bull. Seis. Soc. Am*, 105 (1):300–313, 2015. doi: 10.1785/0120140054.
- Berger, J., Laske, G., Babcock, J., and Orcutt, J. An ocean bottom seismic observatory with near real-time telemetry. *Earth and Space Science*, 3(2):68–77, 2016. doi: 10.1002/2015EA000137.
- Bogiatzis, P., Karamitrou, A., Ward Neale, J., Harmon, N., Rychert, C., and Srokosz, M. Source Regions of Infragravity Waves Recorded at the Bottom of the Equatorial Atlantic Ocean, Using OBS of the PI-LAB Experiment. *Journal of Geophysical Research: Oceans*, 125(6):2019 015430, 2020. doi: 10.1029/2019JC015430.
- Bowden, D., Kohler, M., Tsai, V., and Weeraratne, D. Off-shore Southern California lithospheric velocity structure from noise cross-correlation functions. *Journal of Geophysical Research: Solid Earth*, 121(5):3415–3427, 2016. doi: 10.1002/2016JB012919.
- Butler, R., Lay, T., Creager, K., Earl, P., Fischer, K., Gaherty, J., Laske, G., Leith, B., Park, J., Ritzwolle, M., Tromp, J., and Wen, L. The global seismographic network surpasses its design goal. *Eos, Transactions American Geophysical Union*, 85(23):225–229, 2004. doi: 10.1029/2004EO230001.
- Bécel, A., Laigle, M., Diaz, J., Montagner, J.-P., and Hirn, A. Earth's free oscillations recorded by free-fall OBS ocean-bottom seismometers at the Lesser Antilles subduction zone. *Geophysical Research Letters*, 38(24), 2011. doi: 10.1029/2011GL049533.
- Cox, C., Deaton, T., and Webb, S. A Deep-Sea Differential Pressure Gauge. *Journal of Atmospheric and Oceanic Technology*, 1(3): 237–246, 1984. doi: 10.1175/1520-0426(1984)001.
- Crawford, W. and Webb, S. Identifying and Removing Tilt Noise from Low-Frequency (<0.1 Hz) Seafloor Vertical Seismic Data. *Bull. Seismol. Soc. Am*, 90(4):952–963, 2000.
- Dahlen, F. The effect of data windows on the estimation of free oscillation parameters. *Geophys. J. Int*, 69(2):537–549, 1982. doi: 10.1111/j.1365-246X.1982.tb04964.x.
- Dahlen, F. and Tromp, J. *Theoretical Global Seismology*. Princeton University Press, 1998.
- Deen, M., Wielandt, E., Stutzmann, E., Crawford, W., Barruol, G., and Sigloch, K. First Observation of the Earth's Permanent Free Oscillations on Ocean Bottom Seismometers. *Geophysical Research Letters*, 44(21):10,988–910,996, 2017. doi: 10.1002/2017GL074892.
- Duennebier, F., Harris, D., Jolly, J., Caplan-Auerbach, J., Jordan, R., Copson, D., Stiffel, K., Babinec, J., and Bosel, J. HUGO: the Hawaii Undersea Geo-Observatory. *IEEE Journal of Oceanic Engineering*, 27(2):218–227, 2002. doi: 10.1109/JOE.2002.1002476.
- Dziewonski, A. and Anderson, D. Preliminary Reference Earth Model. *Physics of the Earth and Planetary Interiors*, 25(4): 297–356, 1981.
- Fischer, K., Rychert, C., Dalton, C., Miller, M., Beghein, C., and Schutt, D. A comparison of oceanic and continental mantle lithosphere. *Physics of the Earth and Planetary Interiors*, 309: 106600, 2020. doi: 10.1016/j.pepi.2020.106600.
- Gilbert, F. and Dziewonski, A. An application of normal mode theory to the retrieval of structural parameters and source mechanisms from seismic spectra. *Philosophical Transactions of the Royal Society of London. Series A, Mathematical and Physical Sciences*, 278(1280):187–269, 1975. doi: 10.1098/rsta.1975.0025.
- Harmon, N., Rychert, C., Agius, M., Tharimena, S., Le Bas, T., Kendall, J., and Constable, S. Marine geophysical investigation of the Chain Fracture Zone in the equatorial Atlantic from the PI-LAB Experiment. *J. Geophys. Res*, 123:11,016–011,030, 2018. doi: 10.1029/2018JB015982.
- Harmon, N., Rychert, C., Kendall, J., Agius, M., Bogiatzis, P.,

- and Tharimena, S. Evolution of the Oceanic Lithosphere in the Equatorial Atlantic From Rayleigh Wave Tomography, Evidence for Small-Scale Convection From the PI-LAB Experiment. *Geochemistry Geophysics Geosystems*, 21(9), 2020. doi: 10.1029/2020GC009174.
- Harmon, N., Wang, S., Rychert, C., Constable, S., and Kendall, J. Shear Velocity Inversion Guided by Resistivity Structure From the PI-LAB Experiment for Integrated Estimates of Partial Melt in the Mantle. *Journal of Geophysical Research: Solid Earth*, 126 (8):2021 022202, 2021. doi: 10.1029/2021JB022202.
- Hicks, S., Okuwaki, R., Steinberg, A., Rychert, C., Harmon, N., Abercrombie, R., Bogiatzis, P., Schlaphorst, D., Zahradnik, J., Kendall, J., Yagi, Y., Shimizu, K., and Sudhaus, H. Backpropagating supershear rupture in the 2016 Mw 7.1 Romanche transform fault earthquake. *Nature Geoscience*, 2020. doi: 10.1038/s41561-020-0619-9.
- Kohler, M., Hafner, K., Park, J., Irving, J., Caplan-Auerbach, J.,
 Collins, J., Berger, J., Tréhu, A., Romanowicz, B., and Woodward,
 R. A Plan for a Long-Term, Automated, Broadband Seismic Monitoring Network on the Global Seafloor. Seismological Research Letters, 91(3):1343–1355, 2020. doi: 10.1785/0220190123.
- Laske, G. Observations of Earth's Normal Modes on Broadband Ocean Bottom Seismometers [Original Research. *Frontiers in Earth Science*, 9, 2021. doi: 10.3389/feart.2021.679958.
- Laske, G. and Widmer-Schnidrig, R. 1.04 Theory and Observations: Normal Mode and Surface Wave Observations. In Schubert, G., editor, *Treatise on Geophysics*, page 117–167. Elsevier, second edition, 2015. doi: 10.1016/B978-0-444-53802-4.00003-8.
- Leptokaropoulos, K., Harmon, N., Hicks, S., Rychert, C., Schlaphorst, D., and Kendall, J. Tidal Triggering of Microseismicity at the Equatorial Mid-Atlantic Ridge, Inferred From the PI-LAB Experiment. *Journal of Geophysical Research: Solid Earth*, 126(9):2021 022251, 2021. doi: 10.1029/2021JB022251.
- Leptokaropoulos, K., Rychert, C., Harmon, N., and Kendall, J.-M. Seismicity properties of the Chain Transform Fault inferred using data from the PI-LAB experiment. *Earth and Space Science Open Archive*, 35, 2022. doi: 10.1002/essoar.10511418.1.
- Lin, P., Gaherty, J., Jin, G., Collins, J., Lizarralde, D., Evans, R., and Hirth, G. High-resolution seismic constraints on flow dynamics in the ocean asthenosphere. *Nature*, 535:538–541, 2016. doi: 10.1038/nature18012.
- Masters, G., Jordan, T., Silver, P., and Gilbert, F. Aspherical Earth structure from fundamental spheroidal-mode data. *Nature*, 298 (5875):609–613, 1982. doi: 10.1038/298609a0.
- Masters, G., Laske, G., Bolton, H., and Dziewonski, A. The relative behavior of shear velocity, bulk sound speed, and compressional velocity in the mantle: Implications for chemical and thermal structure. *Washington DC American Geophysical Union Geophysical Monograph Series*, 117:63–87, 2000. doi: 10.1029/GM117p0063.
- Masters, T. and Widmer, R. Free Oscillations: Frequencies and Attenuations, 1995.
- Mehouachi, F. and Singh, S. Water-rich sublithospheric melt channel in the equatorial Atlantic Ocean. *Nat. Geosci*, 11:65–69, 2018. doi: 10.1038/s41561-017-0034-z.
- Moulik, P. and Ekström, G. An anisotropic shear velocity model of the Earth's mantle using normal modes, body waves, surface waves and long-period waveforms. *Geophys. J. Int*, 199(3): 1713–1738, 2014. doi: 10.1093/gji/ggu356.
- Ritsema, J., Heijst, H., and Woodhouse, J. Complex shear wave velocity structure imaged beneath Africa and Iceland. *Science*, 286(5446):1925–1928, 1999.

- Ritsema, J., Deuss, A., Heijst, H., and Woodhouse, J. S40RTS: a degree-40 shear-velocity model for the mantle from new Rayleigh wave dispersion, teleseismic traveltime and normal-mode splitting function measurements. *Geophysical Journal International*, 184(3):1223–1236, 2011. doi: 10.1111/j.1365-246X.2010.04884.x.
- Rychert, C., Kendall, J., and Harmon, N. Passive Imaging of the Lithosphere-Asthenosphere Boundary, 2016.
- Rychert, C., Harmon, N., Constable, S., and Wang, S. The Nature of the Lithosphere-Asthenosphere Boundary. *Journal of Geophysical Research-Solid Earth*, 125(10), 2020.
- Rychert, C., Tharimena, S., Harmon, N., Wang, S., Constable, S., Kendall, J., Bogiatzis, P., Agius, M., and Schlaphorst, D. A dynamic lithosphere-asthenosphere boundary near the equatorial Mid-Atlantic Ridge. *Earth and Planetary Science Letters*, 566: 116949, 2021. doi: 10.1016/j.epsl.2021.116949.
- Saikia, U., Rychert, C., Harmon, N., and Kendall, J. Sediment structure at the equatorial mid-atlantic ridge constrained by seafloor admittance using data from the PI-LAB experiment. *Marine Geophysical Research*, 41(1):10 1007 11001–020–09402–0, 2020.
- Saikia, U., Rychert, C., Harmon, N., and Kendall, J. Upper Mantle Anisotropic Shear Velocity Structure at the Equatorial Mid-Atlantic Ridge Constrained by Rayleigh Wave Group Velocity Analysis From the PI-LAB Experiment. *Geochemistry, Geophysics, Geosystems*, 22(3):2020 009495, 2021a. doi: 10.1029/2020GC009495.
- Saikia, U., Rychert, C., Harmon, N., and Michael Kendall, J. Seismic Attenuation at the Equatorial Mid-Atlantic Ridge Constrained by Local Rayleigh Wave Analysis From the PI-LAB Experiment. *Geochemistry, Geophysics, Geosystems*, 22(12):2021 010085, 2021b. doi: 10.1029/2021GC010085.
- Schlaphorst, D., Rychert, C., Harmon, N., Hicks, S., Bogiatzis, P., Kendall, J., and Abercrombie, R. Local seismicity around the Chain Transform Fault at the Mid-Atlantic Ridge from OBS observations. *Earth and Space Science Open Archive*, 38, 2022. doi: 10.1002/essoar.10511147.1.
- Smith, M. and Masters, G. Aspherical structure constraints from free oscillation frequency and attenuation measurements. Journal of Geophysical Research: Solid Earth, 94(B2):1953–1976, 1989. doi: 10.1029/JB094iB02p01953.
- Stephen, R., Spiess, F., Collins, J., Hildebrand, J., Orcutt, J., Peal, K., Vernon, F., and Wooding, F. Ocean Seismic Network Pilot Experiment. *Geochemistry, Geophysics, Geosystems*, 4(10), 2003. doi: 10.1029/2002GC000485.
- Wang, S., Constable, S., Reyes-Ortega, V., and Rychert, C. A newly distinguished marine magnetotelluric coast effect sensitive to the lithosphere-asthenosphere boundary. *Geophys. J. Int*, 218 (2):978–987, 2019. doi: 10.1093/gji/ggz202.
- Wang, S., Constable, S., Rychert, C., and Harmon, N. A Lithosphere-Asthenosphere Boundary and Partial Melt Estimated Using Marine Magnetotelluric Data at the Central Middle Atlantic Ridge. *Geochemistry Geophysics Geosystems*, 21(9), 2020. doi: 10.1029/2020GC009177.
- Webb, S. and Crawford, W. Long-period seafloor seismology and deformation under ocean waves. *Bull. Seis. Soc. Am*, 89(6): 1535–1542, 1999.
- Wolfe, C., Solomon, S., Laske, G., Collins, J., Detrick, R., Orcutt, J., Bercovici, D., and Hauri, E. Mantle shear-wave velocity structure beneath the Hawaiian hotspot. *Science*, 326:1388–1390, 2009.
- Woodhouse, J. and Dziewonski, A. Mapping the upper mantle: Three-dimensional modeling of earth structure by inversion of seismic waveforms. *Journal of Geophysical Research: Solid Earth*, 89(B7):5953–5986, 1984. doi: 10.1029/JB089iB07p05953.

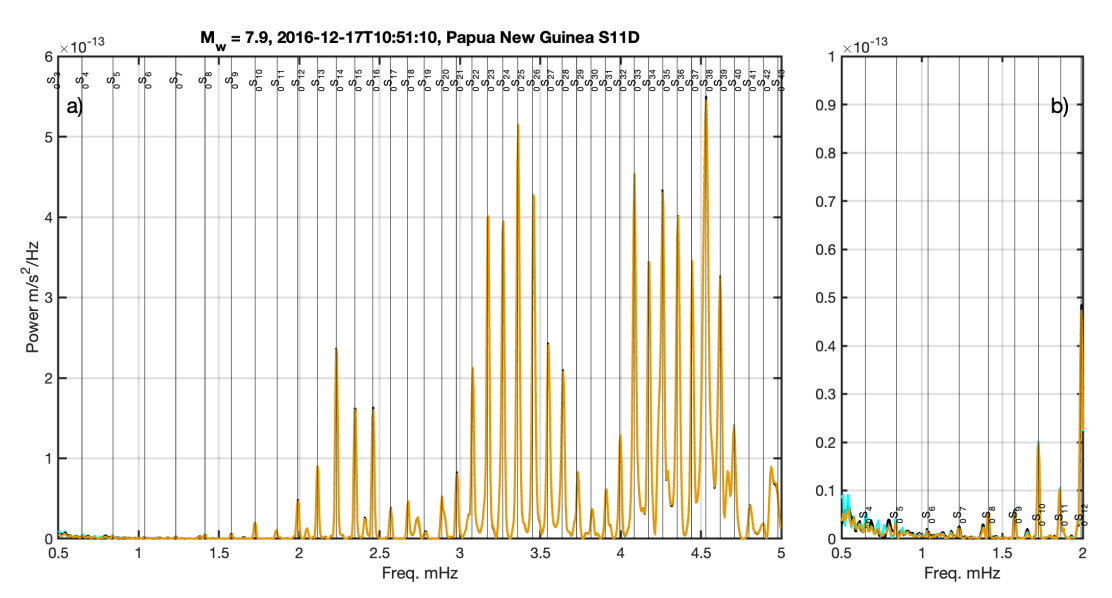


Figure S1. Example spectra after the application of tilt and compliance corrections for the 2016 event to station S11D which had a tilt of 0.13° . a) The spectra from 0.5-5.0 mHz and b) a zoom of 0.5-2.0 mHz are shown. In both panels, the black lines show the spectra of the uncorrected data. The blue line (visible in b) near $_0S_4$) shows the tilt response corrected data. The orange line shows the tilt and compliance corrected data. The blue and orange lines are nearly identical, with the largest difference observed at $_0S_9$. The cyan line shows the result from the spectral tilt correction (Bell et al., 2015; W. C. Crawford & S. C. Webb, 2000). Global average fundamental mode frequencies are shown by thin vertical lines, and modes are labeled (Masters and Widmer, 1995)

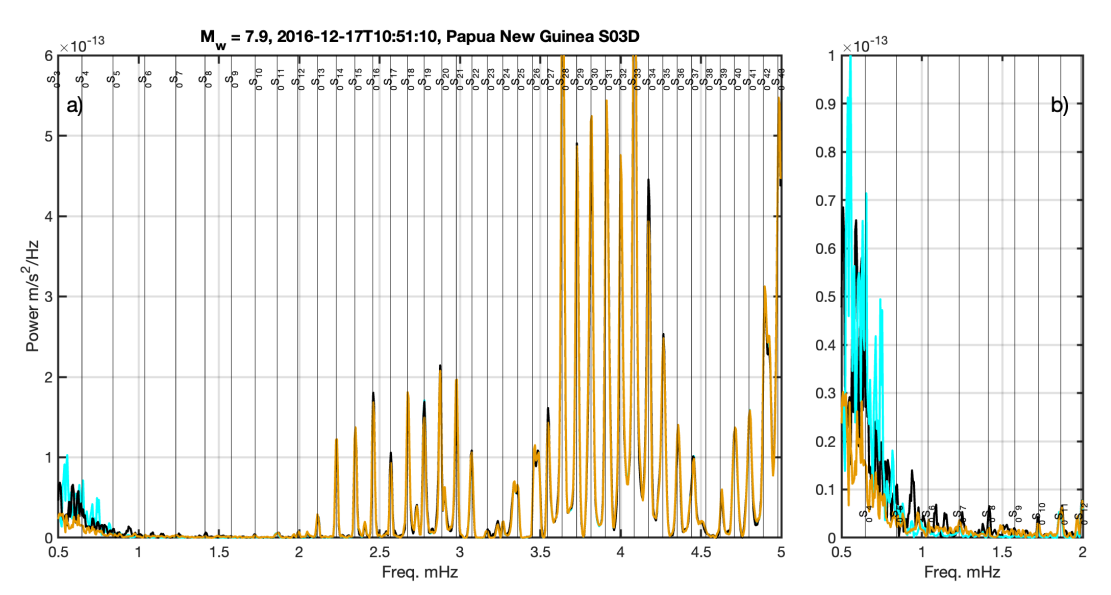


Figure S2. Example spectra after the application of tilt and compliance corrections for the 2016 event to station S03D which had a tilt of 0.48° . a) The spectra from 0.5-5.0 mHz and b) a zoom of 0.5-2.0 mHz are shown. In both panels, the black lines show the spectra of the uncorrected data. The blue line (visible in b) near $_{0}S_{4}$) shows the tilt response corrected data. The orange line shows the tilt and compliance corrected data. The blue and orange lines are nearly identical, with the largest difference observed at $_{0}S_{9}$. The cyan line shows

the result from the spectral tilt correction (Bell et al., 2015; W. C. Crawford & S. C. Webb, 2000). Global average fundamental mode frequencies are shown by thin vertical lines, and modes are labeled (Masters and Widmer. 1995)

Matlab Function for Rotational Tilt Correction

```
%this function will determine the best fitting tilt direction and amount
bv
%minimizing energy on the vertical component.
%input are X(east), Y(north) and Z(vertical).
%output are Znew (tilt corrected Z), Xnew (rotated X), Ynew (rotated Y),
%angy (azimuthal rotation in degrees) and vrt (tilt angle from vertical in
%Note this operates on the second half of the time series-can be modified
%as need to operate on whole time series, etc by modifying inline function
%ff below.
%requires optimization toolbox
function [Znew,angy,vrt,Xnew,Ynew] = tilt corr rot(X,Y,Z);
%% first do polarization analysis on the data to get a guess of the tilt
direction.
                   S=cov([Z(end-length(Z)/2:end) X(end-length(Z)/2:end) Y(end-
length(Z)/2:end)]);
                   [V,D]=eig(S);
                   linny=1-(D(2,2)+D(1,1))/2/D(3,3);
                   planny=1-2*D(1,1)/(D(2,2)+D(3,3));
                   if linny>0.1 %this is a relatively linear phase recorded
                           %calculate the rotation angle
                           angy=atan(V(3,3)*sign(V(1,3))/(V(2,3)))*180/pi;
                   end
%% search for the best fitting azimuth (angy) and tilt (vrt)
                   [\sim, idd] = max(abs(V(1,:)));
                   vrt=acosd(V(1,idd));
                   ff=0(x)Zrot(Z(end-length(Z)/2:end),X(end-length(Z)/2:end),Y(end-length(Z)/2:end),Y(end-length(Z)/2:end),Y(end-length(Z)/2:end),Y(end-length(Z)/2:end),Y(end-length(Z)/2:end),Y(end-length(Z)/2:end),Y(end-length(Z)/2:end),Y(end-length(Z)/2:end),Y(end-length(Z)/2:end),Y(end-length(Z)/2:end),Y(end-length(Z)/2:end),Y(end-length(Z)/2:end),Y(end-length(Z)/2:end),Y(end-length(Z)/2:end),Y(end-length(Z)/2:end),Y(end-length(Z)/2:end),Y(end-length(Z)/2:end),Y(end-length(Z)/2:end),Y(end-length(Z)/2:end),Y(end-length(Z)/2:end),Y(end-length(Z)/2:end),Y(end-length(Z)/2:end),Y(end-length(Z)/2:end),Y(end-length(Z)/2:end),Y(end-length(Z)/2:end),Y(end-length(Z)/2:end),Y(end-length(Z)/2:end),Y(end-length(Z)/2:end),Y(end-length(Z)/2:end),Y(end-length(Z)/2:end),Y(end-length(Z)/2:end),Y(end-length(Z)/2:end),Y(end-length(Z)/2:end),Y(end-length(Z)/2:end),Y(end-length(Z)/2:end),Y(end-length(Z)/2:end),Y(end-length(Z)/2:end),Y(end-length(Z)/2:end),Y(end-length(Z)/2:end),Y(end-length(Z)/2:end),Y(end-length(Z)/2:end),Y(end-length(Z)/2:end),Y(end-length(Z)/2:end),Y(end-length(Z)/2:end),Y(end-length(Z)/2:end),Y(end-length(Z)/2:end),Y(end-length(Z)/2:end),Y(end-length(Z)/2:end),Y(end-length(Z)/2:end),Y(end-length(Z)/2:end),Y(end-length(Z)/2:end),Y(end-length(Z)/2:end),Y(end-length(Z)/2:end),Y(end-length(Z)/2:end),Y(end-length(Z)/2:end),Y(end-length(Z)/2:end),Y(end-length(Z)/2:end),Y(end-length(Z)/2:end),Y(end-length(Z)/2:end),Y(end-length(Z)/2:end),Y(end-length(Z)/2:end),Y(end-length(Z)/2:end),Y(end-length(Z)/2:end),Y(end-length(Z)/2:end),Y(end-length(Z)/2:end),Y(end-length(Z)/2:end),Y(end-length(Z)/2:end),Y(end-length(Z)/2:end),Y(end-length(Z)/2:end),Y(end-length(Z)/2:end),Y(end-length(Z)/2:end),Y(end-length(Z)/2:end),Y(end-length(Z)/2:end),Y(end-length(Z)/2:end),Y(end-length(Z)/2:end),Y(end-length(Z)/2:end),Y(end-length(Z)/2:end),Y(end-length(Z)/2:end),Y(end-length(Z)/2:end),Y(end-length(Z)/2:end),Y(end-length(Z)/2:end),Y(end-length(Z)/2:end),Y(end-length(Z)/2:end),Y(end-length(Z)/2:end),Y(end-length(Z)/2:end),Y(end-length(Z)/2:end),Y(end-le
length(Z)/2:end),x);
                   options=optimset('Display','iter');
                   warning off
                   [vrt,zvr2]=fminsearch(ff,[vrt;angy]);
                   angy=vrt(2);
                   vrt=vrt(1);
                   [Znew, Ynew, Xnew] = xyzrot(X,Y,Z,[vrt;angy]);
end
function zvr = Zrot(Z,X,Y,vrt)
[Znew, ynew, xnew] = xyzrot(X,Y,Z,vrt);
zvr=sqrt(Znew(:)'*Znew(:));
end
function [znew,ynew,xnew]=xyzrot(x,y,z,tst)
vrt=tst(1);angy=tst(2);
dipZ=-90+vrt;%sin change on vrt due to how it is determined
dipY=vrt*cosd(angy);
dipX=vrt*sind(angy);
%make vectors from dip and azimuth
zv=[-sind(dipZ);cosd(dipZ).*cosd(angy);sind(angy).*cosd(dipZ)];
yv=[-sind(dipY);cosd(dipY).*cosd(0);sind(0).*cosd(dipY)];
xv=[-sind(dipX);cosd(dipX).*cosd(90);sind(90).*cosd(dipX)];
C=[zv yv xv];
jk=inv(C)*[z y x]';
```

```
znew=jk(1,:)';
ynew=jk(2,:)';
xnew=jk(3,:)';
end
```